Chinese Journal of Electronics
vol. 33, no. 2, pp. 479–487, March 2024
https://doi.org/10.23919/cje.2022.00.328

RESEARCH ARTICLE

The Establishment and Analysis of the Structural-Electromagnetic Coupling Model of the Electrostatically Controlled Deployable Membrane Antenna

Shunji ZHANG[1,2], Yongzhen GU[1], Wang ZHONG[2], and Qinggang ZHANG[1]

1. *Qingdao University of Science and Technology, Qingdao 266061, China*
2. *Key Laboratory of Electronic Equipment Structure Design of Ministry of Education, Xidian University, Xi'an 710071, China*

Corresponding author: Yongzhen GU, Email: yzgu@qust.edu.cn
Manuscript Received September 28, 2022; Accepted April 7, 2023

Abstract — A new structural-electromagnetic coupling (SEC) analysis based on quadratic elements is proposed to solve the mismatch problem between structural elements and electromagnetic grids of the electrostatically controlled deployable membrane antenna (ECDMA). Firstly, the ECDMA reflector surface is meshed and redefined by a series of quadratic elements. Without grid transformation, the calculating formulas for the far-field pattern of ECDMA are derived by the physical-optics method. Then the structural deformation of ECDMA is analyzed and the far-field pattern calculating formulas including deformation errors are developed. Simulation and experiment results show that the quadratic elements are effective and efficient in SEC analysis of the ECDMA, moreover, the electromagnetic grid size demand and the grid discretization error are reduced greatly.
Keywords — Membrane antenna, Structural-electromagnetic coupling model, Quadratic elements.
Citation — Shunji ZHANG, Yongzhen GU, Wang ZHONG, *et al.*, "The Establishment and Analysis of the Structural-Electromagnetic Coupling Model of the Electrostatically Controlled Deployable Membrane Antenna," *Chinese Journal of Electronics*, vol. 33, no. 2, pp. 479–487, 2024. doi: 10.23919/cje.2022.00.328.

I. Introduction

With the rapid development of space science and technology, space reflector antennas have been widely used in aerospace, communication, remote sensing, and radio astronomy [1]–[3]. There are growing trends to be large diameter, lightweight, and high accuracy of antennas, therefore, the design requirements of space reflector antennas become more demanding. The structural health monitoring and modal updating for space-borned antennas on orbit are also necessary [4]–[6]. As a kind of space-borned reflector antenna, the electrostatically controlled deployable membrane antenna (ECDMA) has been one of the most potential space structures for the 21st Century due to its advantages: the large aperture and light weight are guaranteed by its deployable structure and membrane material, high surface precision is ensured by electrostatic forces active control [7]–[9]. It should be noticed that the membrane surface will cause large deformation under external loads, in particular, temperature loads in space. On the one hand, large deformation will change electrostatic forces, on the other hand, it will affect the far-field pattern of the ECDMA. The structural-electromagnetic coupling (SEC) analysis for ECDMA is of great significance to understand the overall antenna performance.

At present, the SEC method has been widely applied to the reflector antenna design, and one of the biggest challenges is the structural elements and electromagnetic grids mismatch problem. In general, the size of structural elements is much larger than that of electromagnetic grids, because in traditional electromagnetic analysis the size of the grids should be less than to $\lambda/8$ (λ is the wavelength) [10]. The errors of reflector antenna

Associate Editor: Prof. Meisong TONG, Tongji University.

obtained by structural analysis cannot be directly introduced into the electromagnetic analysis. There are two traditional solutions to this problem: 1) a new reflector surface is fitted from the structural elements then the electromagnetic grids can mesh on the new surface, however, the structure errors cannot be accurately reflected in the electromagnetic analysis; 2) the electromagnetic grids are meshed on the structural elements directly, in this method the structural elements are usually plane and the grid discretization errors will be introduced especially in the high-frequency analysis. To solve this problem, Li *et al.* [11], [12] proposed a grid conversion method by selecting Gauss integration points inside each structural element instead of refining the structural elements, the displacement of internal calculating points is obtained by the finite element linear shape functions interpolation. This method improved the electromagnetic analysis, however, the internal calculating points are on the planer structural element which has no benefit in reducing grid discretization errors. Noticing the problem, Lian *et al.* [13] came up with a mesh refinement method of structural elements to produce electromagnetic grids by constructing a quadratic surface over each element. The quadratic surface was constructed through element vertices' coordinates and normal vectors, which were constructed through linear combination of the adjacent elements' normal vectors. In addition, Zhang *et al.* [14] proposed an approximation radiation integral method for distorted reflector antennas using decomposition orthogonal basis functions. The proposed method can benefit the repeated calculations for a given reflector in shaped reflector design and the integrated optimization design. Based on the concept of structural-electromagnetic field coupling, Zhang *et al.* [14] developed an approximation method to analyze the radiation pattern for distorted reflector. In this method, the integration point deformation is obtained by a local interpolation scheme which utilized the same function as that in the structural analysis for the radiation calculation, however, the triangular element is still not conducive to reducing the grid discretization errors. Moreover, Liu *et al.* [15] and Gu *et al.* [16] have studied the electrostatic field and membrane displacement field coupling problems in the ECDMA, however, the electromagnetic field is not involved.

In general, the theoretical research on structural-electromagnetic field coupling problem of reflector antenna has been relatively mature, however, there is a lack of research on how to use the same grid for structural analysis and electromagnetic analysis without introducing discrete errors. To solve this problem, we proposed a SEC analysis method for reflector antenna based on the quadratic finite elements. In Section Ⅱ, the method of electromagnetic analysis using six-node triangular elements is expounded theoretically. The SEC relationship between the electrostatic field, membrane structural displacement field, and the electromagnetic field is analyzed in Section Ⅲ. The effectiveness and correction of this method are verified by simulation and experiment in Section Ⅳ.

II. The Physical-Optics Method by Quadratic Elements

Unlike traditional reflector antennas, the ECDMA is a more complex coupling system. In this section, the electromagnetic field analysis of the ECDMA is developed. The physical-optics (PO) method provides a very accurate solution for predicting the far-field pattern of the reflector antennas in the main beam region and out to several side lobes, therefore, we derive formulas based on the PO method. The PO formulation can be constructed using the steps described in reference [17]. The final can be expressed as (see Figure 1),

$$\boldsymbol{E}(\theta,\phi) = -\mathrm{j}k\eta\frac{\mathrm{e}^{-\mathrm{j}kr}}{4\pi r}(\hat{\boldsymbol{I}} - \hat{\boldsymbol{r}}\hat{\boldsymbol{r}})\cdot\boldsymbol{T}(\theta,\phi) \tag{1}$$

$$\boldsymbol{T}(\theta,\phi) = \iint_S \boldsymbol{J}(\boldsymbol{r'})\mathrm{e}^{\mathrm{j}k\boldsymbol{r'}\cdot\hat{\boldsymbol{r}}}\,\mathrm{d}S \tag{2}$$

$$\boldsymbol{J}(\boldsymbol{r'}) = 2\hat{\boldsymbol{n}}\times\boldsymbol{H}^i \tag{3}$$

where $\mathrm{j}=\sqrt{-1}$, $k=2\pi/\lambda$, λ is the wavelength, η =120π, r is the distance between the far-field point and the origin of coordinates, $\hat{\boldsymbol{I}}$ is the unit dyad, $\hat{\boldsymbol{r}}\hat{\boldsymbol{r}}$ the dyad of the far-field point directional unit vector $\hat{\boldsymbol{r}}$, S is the reflector surface of the ECDMA, $\boldsymbol{r'}$ is the position vector of reflector surface point, moreover, the unit outward normal vector of the surface at this point is $\hat{\boldsymbol{n}}$, $\boldsymbol{J}(\boldsymbol{r'})$ is the physical-optics current at the reflector surface, $\boldsymbol{H}^i$ is the incoming magnetic field vector. The reflector surface and far-field both are defined in the global coordinate system (x,y,z), the feed source is defined in the local coordinate system (x_s,y_s,z_s), $\boldsymbol{r}$ is the far-field point directional vector, $\boldsymbol{r}^s$ is the reflector surface point directional vector in coordinates (x_s,y_s,z_s), $\boldsymbol{s}$ is the feed directional vector in the coordinate system (x,y,z). It can be seen from Figure 1, when $\boldsymbol{r}^s=\boldsymbol{0}$, the ECDMA is an axis-symmetrical reflector antenna.

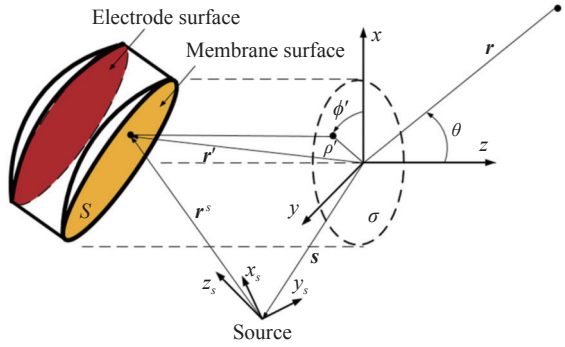

Figure 1 The schematic diagram of the ECDMA in coordinate systems.

As long as the feed information and the reflector shape are given, we can obtain the far-field pattern of the reflector antenna through (1)–(3). In practical terms, the

reflector surface has system errors and random errors, making a not ideal parabolic. The surface should be meshed by plane triangular elements, then the electromagnetic field analysis is based on the mesh, such as refining the mesh or selecting Gauss integration points inside each element traditionally. However, they cannot reduce the grid discretization errors radically. For the problem, we mesh the reflector surface by a series of six-node triangular elements and each of them can be expressed by a quadratic surface equation. Taking the i-th element for example (see Figure 2), the coordinate value z_i of z-axis direction of point in the i-th element can be expressed as

$$z_i = a_{i0} + a_{i1}x + a_{i2}y + a_{i3}xy + a_{i4}x^2 + a_{i5}y^2 \quad (4)$$

where x and y are the coordinate value of x- and y-axis direction of point, respectively, $a_{i0} - a_{i5}$ are unknown coefficients. Because this element is part of a paraboloid, therefore, it is a quadratic surface element. We know that each element has 6 nodes, substituting their coordinates into (4) respectively, the unknown coefficients can be obtained by solving simultaneous equations.

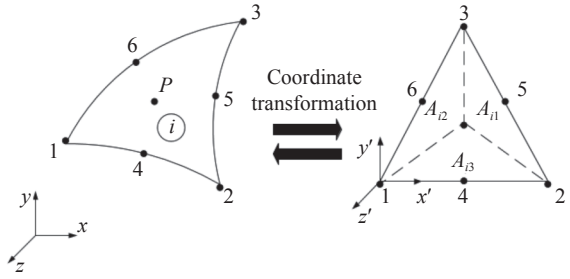

Figure 2 A six-node triangular element in global and local coordinate systems.

In order to avoid solving simultaneous equations, we can take advantage of the shape functions of the finite element method to acquire the location coordinates of every point (such as P in Figure 2) in this element directly:

$$\boldsymbol{r'}_i = \sum_{j=1}^{6} N_{ij}\boldsymbol{r'}_{ij} \quad (5)$$

where $\boldsymbol{r'}_{ij}$ is the global coordinates of the j-th node in the i-th six-node triangular element, N_{ij} is the shape functions corresponding to the element which can be obtained as

$$N_{ij} = \begin{cases} L_{ij}(2L_{ij} - 1), \ j = 1, 2, 3 \\ 4L_{im}L_{in}, \ j = 4, 5, 6, \ m = 1, 2, 3, \ n = 2, 3, 1 \end{cases} \quad (6)$$

in which, $L_{ij} = \frac{A_{ij}}{A_i}$ $(j = 1, 2, 3)$ are the area coordinates of triangular, they can be obtained easily in the element local coordinates. Substituting (5) and (6) into (2) and (3), we can rewrite the PO formulation based on six-node triangular surface integrals as follows:

$$\boldsymbol{T}(\theta, \phi) = \sum_{i=1}^{\mathrm{NUM}} \iint_{S_i} \boldsymbol{J}(\boldsymbol{r'}) \mathrm{e}^{\mathrm{j}k\boldsymbol{r'}\cdot\hat{\boldsymbol{r}}} \, \mathrm{d}S_i \quad (7)$$

$$\boldsymbol{J}(\boldsymbol{r'}_i) = 2\hat{\boldsymbol{n}}_i \times \boldsymbol{H}^i \quad (8)$$

where NUM is the total number of six-node triangular elements, S_i represents the i-th element surface, $\hat{\boldsymbol{n}}_i$ is the normal unit vector of the S_i which can be developed as

$$\hat{\boldsymbol{n}}_i = \frac{\boldsymbol{N}_i}{\|\boldsymbol{N}_i\|} \quad (9)$$

$$\begin{aligned} \boldsymbol{N}_i &= \sum_{j=1}^{6} (\boldsymbol{N'}_{ij} \cdot \boldsymbol{r'}_{ij}) \\ &= \sum_{j=1}^{6} \left(\left\{ \boldsymbol{N'}_{ij1}\cdot\boldsymbol{r'}_{ij1} \quad \boldsymbol{N'}_{ij2}\cdot\boldsymbol{r'}_{ij2} \quad \boldsymbol{N'}_{ij3}\cdot\boldsymbol{r'}_{ij3} \right\}^{\mathrm{T}} \right) \end{aligned} \quad (10)$$

$$\boldsymbol{N'}_{ij} = \left\{ \frac{\partial N_{ij}}{\partial x} \quad \frac{\partial N_{ij}}{\partial y} \quad \frac{\partial N_{ij}}{\partial z} \right\}^{\mathrm{T}} \quad (11)$$

where $\boldsymbol{N}_i$ is the normal vector of the S_i, $\boldsymbol{N'}_{ij}\cdot\boldsymbol{r'}_{ij}$ represents the multiplication of elements in matrices $\boldsymbol{N'}_{ij}$ and $\boldsymbol{r'}_{ij}$, the subscript 1, 2, 3 of matrix represent the value of each element in the matrix, respectively, $\boldsymbol{N'}_{ij}$ is the normal vector of the j-th node in the i-th six-node triangular element. The detailed derivations of (9)–(11) can be found in [18]. Integration (7) is performed on the reflector surface S, it can be expressed in terms of the projected circular region σ (dotted circle in Figure 1) with the help of the surface Jacobian transformation J_S, then the surface integral is converted to the plane integral:

$$\boldsymbol{T}(\theta, \phi) = \sum_{i=1}^{\mathrm{NUM}} \iint_{\sigma_i} \boldsymbol{J}(\boldsymbol{r'}) \mathrm{e}^{\mathrm{j}k\boldsymbol{r'}\cdot\hat{\boldsymbol{r}}} J_{S_i} \, \mathrm{d}\sigma_i \quad (12)$$

where J_{S_i} can be expressed as

$$J_{S_i} = \sqrt{\boldsymbol{N}_i^{\mathrm{T}} \boldsymbol{N}_i} \quad (13)$$

in which, $\boldsymbol{N}_i$ is the normal vector of the S_i which can be obtained by (7). The square root of $\boldsymbol{N}_i$ means the conversion coefficient from surface integral to plane integral. It can be noted that, although integration in (12) is performed over a planar aperture, the current is still defined on the curved reflector surface. Equation (12) is the radiation integral for the PO formulation based on the six-node triangular elements. There are two numerical integration methods to solve (12): 1) refining the six-node triangular elements with plane triangular grids; 2) selecting Gauss integration points inside each six-node triangular element. The second approach is preferred in this paper.

III. The SEC Analysis of ECDMA

Figure 3 shows the SEC relationship of the ECD-

MA. It is known that the membrane can be deformed by electrostatic forces meanwhile the electrostatic field strength will change by membrane deformation which is a nonlinear and coupling problem. We can get the coupling model of the electrostatic field and membrane structure displacement field from our previous work [16]:

$$\begin{pmatrix} \boldsymbol{K_{uu}}(\boldsymbol{u},\varphi) & \boldsymbol{K_{u\varphi}}(\boldsymbol{u},\varphi) \\ \boldsymbol{K_{\varphi u}}(\boldsymbol{u},\varphi) & \boldsymbol{K_{\varphi\varphi}}(\boldsymbol{u},\varphi) \end{pmatrix} \begin{Bmatrix} \boldsymbol{u} \\ \varphi \end{Bmatrix} = \begin{Bmatrix} \boldsymbol{f} \\ \boldsymbol{q} \end{Bmatrix} \tag{14}$$

in which, $\boldsymbol{K_{uu}}$ and $\boldsymbol{K_{\varphi\varphi}}$ are the mechanical and electrostatic stiffness matrix respectively, $\boldsymbol{K_{u\varphi}}$ and $\boldsymbol{K_{\varphi u}}$ are the coupled stiffness matrix, $\boldsymbol{u}$ and φ are displacement and potential, respectively, $\boldsymbol{f}$ and $\boldsymbol{q}$ are the mechanical forces and electric charges, respectively.

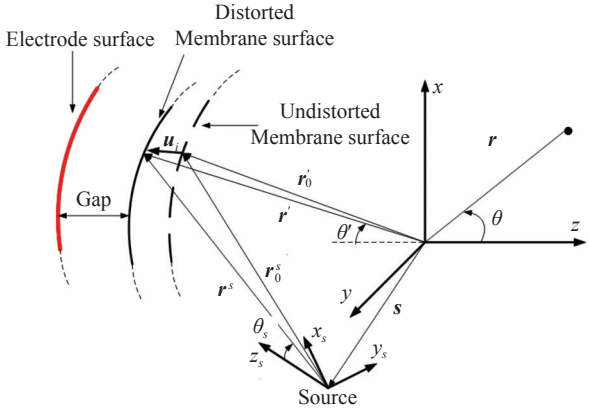

Figure 3 The schematic diagram of SEC relationship in ECDMA.

Solving (14), we can get the ECDMA surface node displacements $\boldsymbol{u}$ which will affect the far-field pattern of the reflector antenna. Some assumptions are made here: 1) the electromagnetic field does not effect the membrane surface; 2) for small-amplitude, smoothly-varying errors, the surface normal $\hat{\boldsymbol{n}}$ will not deviate substantially from that of an undistorted reflector [19]. Then radiation integral for the PO formulation of distorted membrane surface is given by

$$\boldsymbol{T}(\theta,\phi,\boldsymbol{u},\varphi) = \sum_{i=1}^{\mathrm{NUM}} \iint_{\sigma_i} \boldsymbol{J}(\boldsymbol{r'}_{i0}) \mathrm{e}^{\mathrm{j}k\boldsymbol{r'}_{i0}\cdot\hat{\boldsymbol{r}}} \times [\mathrm{e}^{\mathrm{j}ku_{iz}(\cos\theta_s+\cos\theta)}] J_{S_i}\,\mathrm{d}\sigma_i \tag{15}$$

where $\boldsymbol{J}(\boldsymbol{r'}_{i0})\mathrm{e}^{\mathrm{j}k\boldsymbol{r'}_{i0}\cdot\hat{\boldsymbol{r}}}$ is the PO-current term for the undistorted reflector, u_{iz} is the z-axis components of node displacements in the i-th six-node triangular element, θ_s is the direction of the feed pattern which is independent of displacement. The integrand in (15) is a function of both the amplitude and shape of the perturbation function u_{iz}.

The perturbation can be expressed by the six-node triangular element shape functions as,

$$u_{iz} = \sum_{j=1}^{6} N_{ij} u_{ijz} \tag{16}$$

where u_{ijz} is the known z-axis displacement of the j-th node in the i-th element, N_{ij} is the shape function in (6). It is necessary to note that both the ECDMA surface shape and deformation are defined by the same shape functions, making the six-node triangular element a quadratic element. Using a Taylor series, the bracketed exponential from (15) can be expanded as

$$\begin{aligned} &\mathrm{e}^{\mathrm{j}ku_{iz}(\cos\theta_s+\cos\theta)} \\ &\approx 1+\mathrm{j}ku_{iz}(\cos\theta_s+\cos\theta) - k^2u_{iz}^2(\cos\theta_s+\cos\theta)^2/2 \\ &= 1+\mathrm{j}k(\cos\theta_s+\cos\theta)\sum_{j=1}^{6} N_{ij}u_{ijz} \\ &\quad - k^2/2(\cos\theta_s+\cos\theta)^2\Big(\sum_{j=1}^{6} N_{ij}u_{ijz}\Big)^2 \end{aligned} \tag{17}$$

Substituting (16) and (17) into (15), we can divide the radiation integral of the distorted reflector into three parts:

$$\begin{aligned} \boldsymbol{T}(\theta,\phi,\boldsymbol{u},\varphi) = \sum_{i=1}^{\mathrm{NUM}} \Big(&\boldsymbol{T}_0(\theta,\phi) + \Delta\boldsymbol{T}_1(\theta,\phi)u_{ijz} \\ &+ \Delta\boldsymbol{T}_2(\theta,\phi)u_{ijz}u_{imz}\Big) \end{aligned} \tag{18}$$

$$\boldsymbol{T}_0(\theta,\phi) = \sum_{i=1}^{\mathrm{NUM}} \iint_{\sigma_i} \boldsymbol{J}(\boldsymbol{r'}_{i0}) \mathrm{e}^{\mathrm{j}k\boldsymbol{r'}_{i0}\cdot\hat{\boldsymbol{r}}} J_{S_i}\,\mathrm{d}\sigma_i \tag{19}$$

$$\begin{aligned} \Delta\boldsymbol{T}_1(\theta,\phi) = \sum_{i=1}^{\mathrm{NUM}} \iint_{\sigma_i} &\boldsymbol{J}(\boldsymbol{r'}_{i0}) \mathrm{e}^{\mathrm{j}k\boldsymbol{r'}_{i0}\cdot\hat{\boldsymbol{r}}} \cdot \mathrm{j}k(\cos\theta_s+\cos\theta) \\ &\cdot \sum_{j=1}^{6} (N_{ij}) J_{S_i}\,\mathrm{d}\sigma_i \end{aligned} \tag{20}$$

$$\begin{aligned} \Delta\boldsymbol{T}_2(\theta,\phi) = \sum_{i=1}^{\mathrm{NUM}} \iint_{\sigma_i} &\boldsymbol{J}(\boldsymbol{r'}_{i0}) \mathrm{e}^{\mathrm{j}k\boldsymbol{r'}_{i0}\cdot\hat{\boldsymbol{r}}} \cdot \left(-k^2/2\right) \\ &\cdot (\cos\theta_s+\cos\theta)^2 \sum_{j,m=1}^{6} (N_{ij}N_{im}) J_{S_i}\,\mathrm{d}\sigma_i \end{aligned} \tag{21}$$

where $\boldsymbol{T}_0(\theta,\phi)$, $\Delta\boldsymbol{T}_1(\theta,\phi)$ and $\Delta\boldsymbol{T}_2(\theta,\phi)$ are independent of the membrane surface deformation, $\boldsymbol{u}$ and φ are displacement and potential, respectively, $\boldsymbol{J}(\boldsymbol{r'}_{i0})\mathrm{e}^{\mathrm{j}k\boldsymbol{r'}_{i0}\cdot\hat{\boldsymbol{r}}}$ is the PO-current term for the undistorted reflector, J_{S_i} is the surface Jacobian transformation, u_{ijz} and u_{imz} are the nodal displacement. To avoid repeated calculation, we can store the radiation integral for the undistorted reflector $\boldsymbol{T}_0(\theta,\phi)$ and the integration $\Delta\boldsymbol{T}_1(\theta,\phi)$ and $\Delta\boldsymbol{T}_2(\theta,\phi)$. In this way, when we need to calculate the far-field pattern of the distorted reflector antenna, the results can be derived by multiplying $\Delta\boldsymbol{T}_1(\theta,\phi)$ and $\Delta\boldsymbol{T}_2(\theta,\phi)$ with the deformation errors u_{ijz}. Finally, we can divide the radiation integral of distorted reflector based on the SEC model as follows:

$$\boldsymbol{E}(\theta,\phi,\boldsymbol{u},\varphi) = -\mathrm{j}k\eta\frac{\mathrm{e}^{-\mathrm{j}kr}}{4\pi r}(\hat{\boldsymbol{I}}-\hat{\boldsymbol{r}}\hat{\boldsymbol{r}}) \cdot\left(\sum_{i=1}^{\mathrm{NUM}}(\boldsymbol{T}_0(\theta,\phi)+\Delta\boldsymbol{T}_1(\theta,\phi)u_{ijz}+\Delta\boldsymbol{T}_2(\theta,\phi)u_{ijz}u_{imz})\right) \tag{22}$$

IV. Simulations and Experiments

The radiation integral for the PO formulation based on the six-node triangular element is also applicable to the general reflector antenna. To verify the correctness and validity of this method, a classical simulation example is given first, and then this method is applied to the ECDMA SEC analysis.

1) Simulation example 1

The axis-symmetrical reflector antenna is used as a simulation example with focal length $f = 100\lambda$ and diameter $D = 100\lambda$. An analytical feed pattern of the $\cos^q\theta$-type is used with $q = 8$. This gives an edge taper of -9 dB. The working frequency is set to be 2 GHz. In finite element analysis, the size of the structure element is often larger than the electromagnetic grids, and this phenomenon is more obvious with the increase of the antenna frequency. Here the reflector surface is meshed by the plane triangular elements with the size of λ (referenced method) and the six-node curved triangular element with the size of 10λ (proposed method), respectively. The deformation functions in [19] are adopted to describe the element nodal z-direction displacement. The distorted functions are as follows:

$$u_z(\rho',\phi') = 0.05\lambda\sin\left(2\pi\frac{\rho'^2}{(50\lambda)^2}\right) \tag{23}$$

$$u_z(\rho',\phi') = 0.05\lambda\cos\left(10\pi\frac{\rho'^2}{(50\lambda)^2}\right) \tag{24}$$

$$u_z(\rho',\phi') = 0.05\lambda\cos(5\phi') \tag{25}$$

where the variables ρ' and ϕ' designate the polar coordinate components in the projected aperture plane of the reflector.

The distortions in (23)–(25) have been shown in the upper left corner of the Figures 4(b)–(c), respectively. It can be seen from the figures that the three deformations are periodic functions. Figures 4(a)–(d) show the far-field patterns for the undistorted reflector and distorted reflector of three deformation functions, respectively. Each figure has the patterns in plane for the referenced method (dashed line) and the proposed method (solid line). As can be seen from these images, for the cases of undistorted, deformation (23) and deformation (25), the proposed method results agree well with the results of the referenced method. For the case of deformation (24), there are non-negligible errors in side lobes between the proposed method and referenced method. The reason for this result is that the size of the six-node curved triangular element is larger than the period of deformation (24).

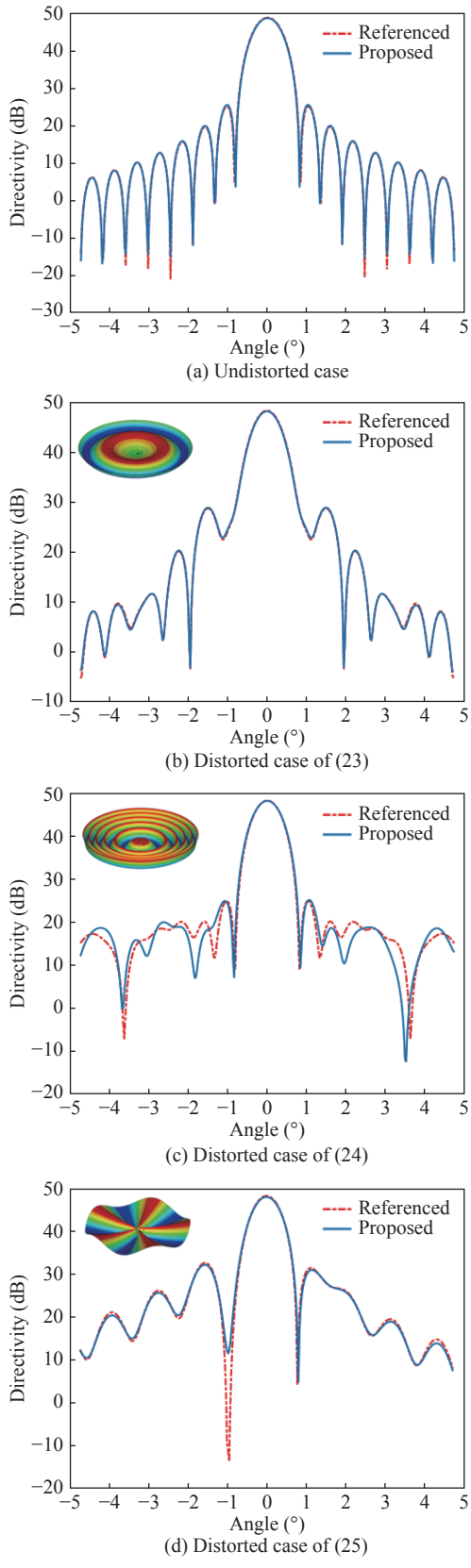

Figure 4 The far-field pattern of the reflector antenna of different cases.

Table 1 lists the max directivity for each pattern. It is concluded that the proposed method results show very good agreement of the referenced method with a maximum error of 0.46%.

Table 1 Maximum directivity for each case

Cases	Undistorted	Deform. (23)	Deform. (24)	Deform. (25)
Referenced	48.99 dB	48.22 dB	48.24 dB	48.15 dB
Proposed	48.86 dB	48.09 dB	48.29 dB	47.93 dB
Error	0.27%	0.27%	0.10%	0.46%

Table 2 lists the computation time for each case. It shows that the proposed method improves the computational efficiency by 96% compared with the referenced method.

Table 2 Time comparison for each pattern

Patterns	Undistorted	Deform. (23)	Deform. (24)	Deform. (25)
Referenced	12.80 s	12.87 s	12.85 s	13.14 s
Proposed	0.51 s	0.51 s	0.51 s	0.49 s
Efficiency	96.0%	96.0%	96.0%	96.3%

2) Simulation example 2

In Section Ⅴ.1, the deformation functions are adopted to describe the element nodal z-direction displacement instead of using the mechanical simulation to obtain the displacement. In this section, an ECDMA model with a diameter of 5 m and a focal length of 10 m are used to the structural-electromagnetic co-simulation. The membrane surface material properties are provided in Table 3.

Table 3 The membrane surface material properties

Young's Modulus	2.17 GPa
Poisson's Ratio	0.34
Thickness	0.025 mm
Density	1432 kg/m^3

The electrodes configuration is demonstrated in Figure 5 which consist of 9 independent electrode voltage channels and the initial distance between membrane surface and electrodes is set as 30 mm. For the sake of simplicity, the membrane surface boundary is set as 0 V and the membrane initial stress is 0.01 MPa, meanwhile, the boundary of the membrane surface is fixed.

The operating electromagnetic frequency of antenna is set as 5 GHz. An analytical feed pattern of the $\cos^q\theta$-type is used with $q = 8$. Here the membrane surface is meshed by the plane triangular (PT) elements with the size of λ and the six-node curved triangular (CT) elements (quadratic elements) with the size of 10λ as shown in Figures 6(a) and (b), respectively. It can be seen from the Figure 6 that in order to reduce the discrete errors of plane approximation to paraboloid, the plane elements need to be divided very closely.

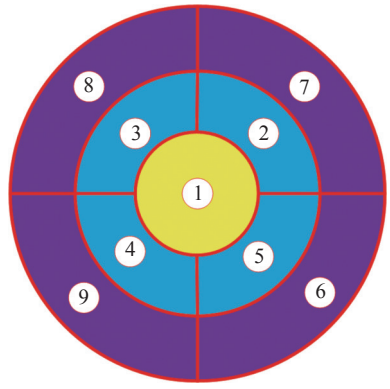

Figure 5 The electrodes configuration.

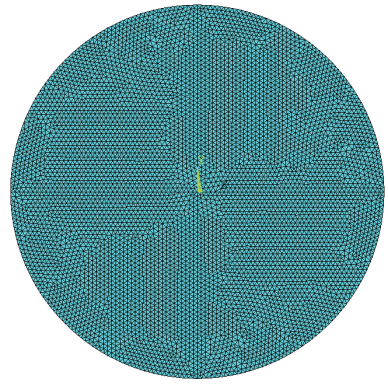

(a) Plane triangular element

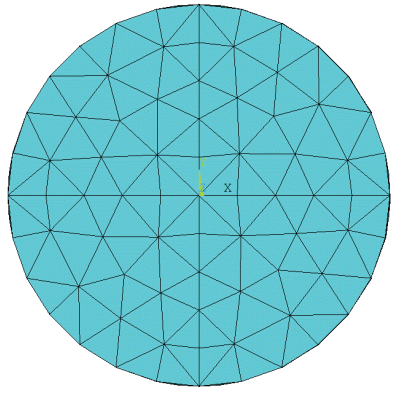

(b) Quadratic elements

Figure 6 The membrane surface mesh.

When the voltages of each channel on the electrode surface is different, the membrane surface will have different deformations. Here we give three cases of electrode voltages as shown in Table 4. Then the membrane surface deformations and far-field patterns of the ECDMA can be obtained by the PT elements and the CT elements, respectively.

Table 4 Maximum directivity for each case

Channels	1	2	3	4	5	6	7	8	9
Case 1 (kV)	10	10	10	10	10	10	10	10	10
Case 2 (kV)	10	6	6	6	6	10	10	10	10
Case 3 (kV)	6	6	6	10	10	10	10	6	6

Figures 7(a), (b) and (c) show the far-field patterns for ECDMA of three cases, respectively. Each figure has the patterns in $\phi = 0°$ plane (E plane) and $\phi = 90°$ plane (H plane) for the referenced method (PT elements) and the proposed method (CT elements). As can be seen from these figures, the proposed method results agree well with the results of the referenced method.

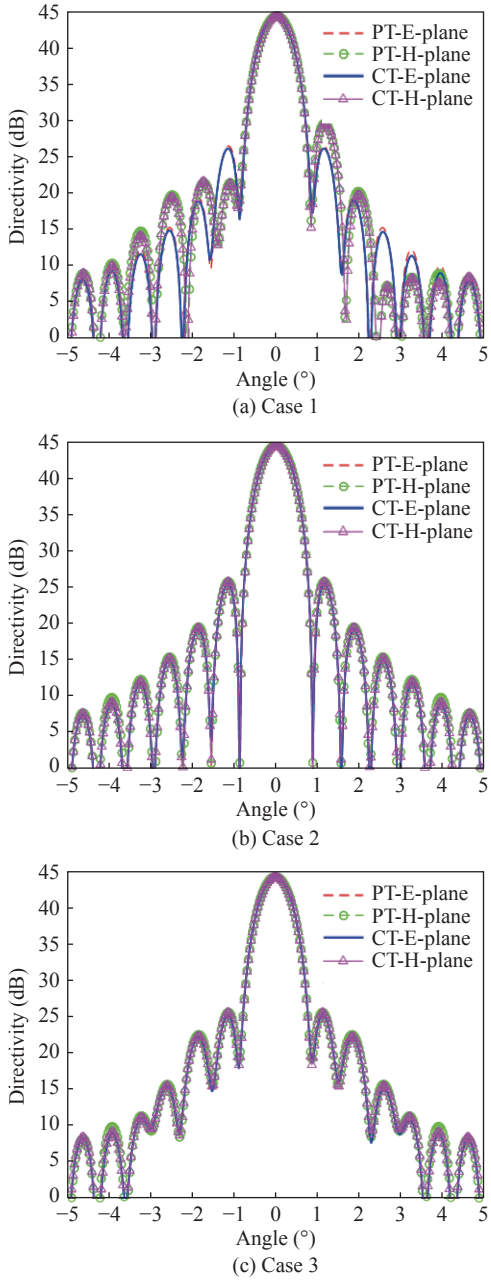

Figure 7 The far-field patterns of the ECDMA with three cases of electrode voltages.

Table 5 lists the max directivity for each pattern. It is concluded that the proposed method results show very good agreement of the referenced method with a maximum error of 0.22%. Table 6 lists the computation time for each case. It shows that the proposed method improves the computational efficiency by about 93.4% compared with the referenced method.

Table 5 Maximum directivity for each case

Cases	Case 1	Case 2	Case 3
Referenced	44.51 dB	44.30 dB	44.30 dB
Proposed	44.41 dB	44.21 dB	44.21 dB
Error	0.22%	0.20%	0.20%

Table 6 Time comparison for each case

Cases	Case 1	Case 2	Case 3
Referenced	124.1 s	137.6 s	141.4 s
Proposed	8.2 s	6.7 s	7.8 s
Efficiency improvement	93.4%	95.1%	94.5%

3) Experiment and results

An ECDMA prototype has been mounted and placed in the laboratory with a focal length of $f = 4$ m and diameter of $D = 1.5$ m. An analytical feed pattern of the $\cos^q\theta$-type is used as $q = 8$. The working frequency is set to be 20 GHz.

There are random errors and system errors in the process of making the ECDMA prototype, therefore, the deviation of the membrane surface to the designed shape is very irregular and cannot be expressed by periodic functions. In that case, the membrane shape is established with the photogrammetry data instead of the ideal design data here. The targets on the ECDMA are shown in Figure 8 and the 3D coordinates of all targets are obtained by the V-STARS industrial photogrammetry system. Then the errors distribution of the ECDMA can be obtained by calculating the errors between the measuring points and the ideal paraboloid. Here we mainly consider the error in the Z-axis direction and the deformation errors can be defined as

$$\Delta z_i = z_i - \frac{x_i^2 + y_i^2}{4f} \tag{26}$$

where (x_i, y_i, z_i) is the 3D coordinates of targets, f is the focal length of the ideal paraboloid.

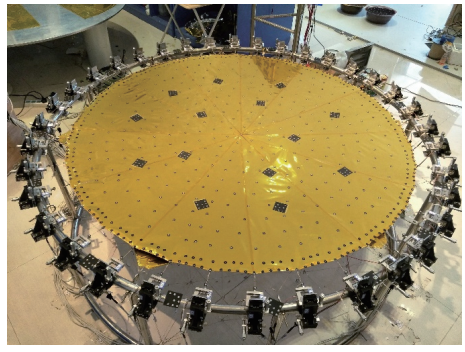

Figure 8 The ECDMA prototype with photogrammetry targets.

Figure 9(a) is the distribution of the ECDMA membrane surface initial errors, it can be seen that the shape of the reflector surface is prominent in the middle and

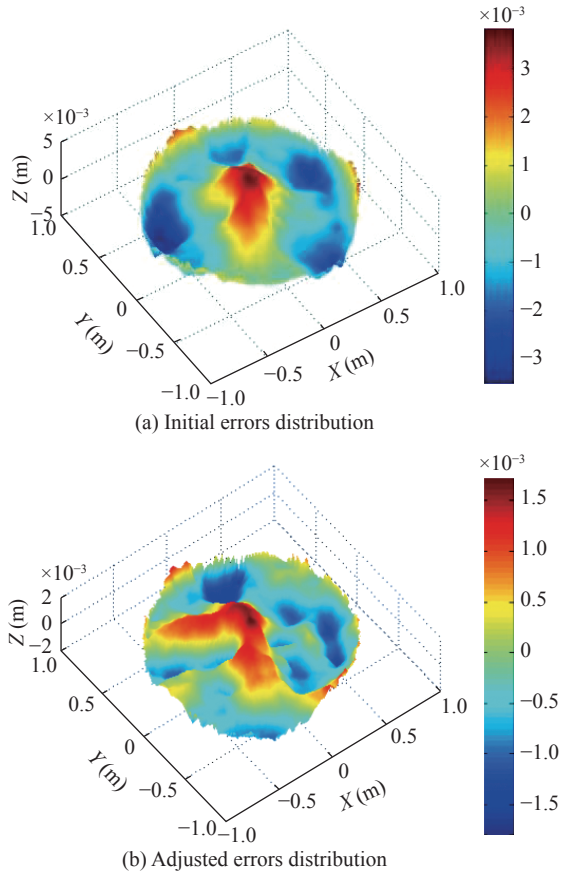

Figure 9 Deformation errors of the ECDMA.

depressed in the surrounding with an amplitude about. To improve the precision of the ECDMA surface we need to adjust the electrode voltages or membrane boundary, here the optimized results are given directly. The adjusted errors distribution are shown in Figure 9(b) and the errors amplitude becomes to be about. Substituting the initial and adjusted errors into (22), respectively, we can get the initial and adjusted far-field pattern of the ECDMA as shown in Figure 10. From the results we can know that the initial errors can seriously reduce the max directivity and raise the side lobe levels, here the max directivity reduces from 43.98 dB to 38.32 dB. In addition,

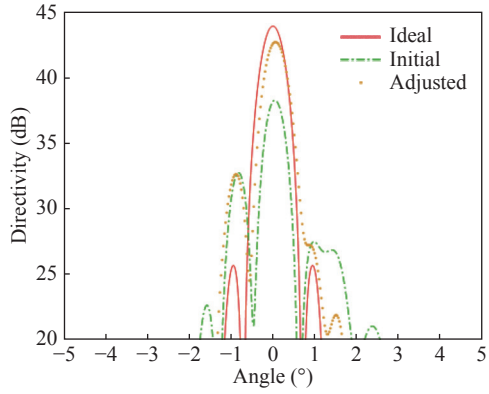

Figure 10 The far-field directivity pattern of ECDMA before and after the adjustment.

the errors can also cause the far-field pattern to be asymmetry. After the adjustment, it is obvious that the max directivity has been improved from 38.32 dB to 42.76 dB.

V. Conclusions

In this study, the calculating formulas for the far-field pattern of the ECDMA are derived based on the quadratic elements. The structural analysis and electromagnetic calculation can share the same grid and avoid discrete errors, therefore, it can improve the calculation efficiency while ensuring the modeling accuracy. The method proposed in this paper is especially suitable for the high-frequency electromagnetic field analysis and structural-electromagnetic optimization design. Moreover, the proposed method is suitable for the small amplitude, smoothly vary errors and can be used in the electrode voltages optimization for the ECMA design of which the radiation performance varies with the structural design variables under exterior forces such as gravity, wind and temperature gradient.

Acknowledgement

This work was supported by the National Natural Sciences Foundation of China (Grant No. 52005277), the Guangdong Fundamentals and Application Fundamentals Research Foundation (Grant No. 2020A1515111043), and the Research Initiation Foundation of Qingdao University of Science and Technology (Grant No. 12030430010878).

References

[1] B. Y. Duan, "Large spaceborne deployable antennas (LSDAs)-a comprehensive summary," *Chinese Journal of Electronics*, vol. 29, no. 1, pp. 1–15, 2020.

[2] M. Chandra, S. Kumar, S. Chattopadhyaya, *et al.*, "A review on developments of deployable membrane-based reflector antennas," *Advances in Space Research*, vol. 68, no. 9, pp. 3749–3764, 2021.

[3] H. Jiang, Y. Yao, T. Xiu, "High-Gain Dual Circularly Polarized Antenna for Air-to-Ground Wireless Link," *Chinese Journal of Electronics*, vol. 31, no. 3, pp. 555–561, 2022.

[4] C. Yang, K. Liang, X. P. Zhang, *et al.*, "Sensor placement algorithm for structural health monitoring with redundancy elimination model based on sub-clustering strategy," *Mechanical Systems and Signal Processing*, vol. 124, pp. 369–387, 2019.

[5] C. Yang, X. B. Hou, and S. N. Chang, "A synchronous placement and size-based multi-objective optimization method for heat dissipation design on antenna module of space solar power satellite," *Sustainable Energy Technologies and Assessments*, vol. 45, article no. 101183, 2021.

[6] C. Yang and H. J. Ouyang, "A novel load-dependent sensor placement method for model updating based on time-dependent reliability optimization considering multi-source uncertainties," *Mechanical Systems and Signal Processing*, vol. 165, article no. 108386, 2022.

[7] S. P. Chodimella, J. D. Moore, and J. Otto, "Design evaluation of a large aperture deployable antenna," in *Proceedings of the 47th AIAA/ASME/ASCE/AHS/ASC Structures, Structural Dynamics, and Materials Conference*, Newport, Rhode Island, 2006.

[8] B. Y. Duan, F. Gao, J. L. Du, *et al.*, "Optimization and experiment of an electrostatic forming membrane reflector in space," *Journal of Mechanical Science and Technology*, vol.

29, no. 4, pp. 1355–1360, 2015.
[9] Y. Q. Zhang, F. Gao, S. X. Zhang, *et al.*, "Electrode grouping optimization of electrostatic forming membrane reflector antennas," *Aerospace Science and Technology*, vol. 41, pp. 158–166, 2015.
[10] FEKO, "User manual, suite 5.3, em software and systems," in *User Manual, Suite 5. 3, EM Software and Systems*, S. A. (Pty) Ltd, 32 Techno Lane, Technopark, Stellenbosch, 7600, South Africa, 2006.
[11] P. Li, B. Y. Duan, W. Wang, *et al.*, "Electromechanical coupling analysis of ground reflector antennas under solar radiation," *IEEE Antennas and Propagation Magazine*, vol. 54, no. 5, pp. 40–57, 2012.
[12] P. Li, N. Li, W. Y. Xu, *et al.*, "Far-field pattern tolerance analysis of reflector antenna with random or system error based on interval arithmetic," *Chinese Journal of Electronics*, vol. 27, no. 3, pp. 641–647, 2018.
[13] P. Y. Lian, B. Y. Duan, W. Wei, *et al.*, "A mesh refinement method of reflector antennas using quadratic surface construction over each structure element," *IEEE Antennas and Wireless Propagation Letters*, vol. 13, pp. 1557–1560, 2014.
[14] S. X. Zhang, B. Y. Duan, G. G. Yang, *et al.*, "An approximation of pattern analysis for distorted reflector antennas using structural-electromagnetic coupling model," *IEEE Transactions on Antennas and Propagation*, vol. 61, no. 9, pp. 4844–4847, 2013.
[15] C. Liu, G. G. Yang, and Y. Q. Zhang, "Optimization design combined with coupled structural–electrostatic analysis for the electrostatically controlled deployable membrane reflector," *Acta Astronautica*, vol. 106, pp. 90–100, 2015.
[16] Y. Z. Gu, B. Y. Duan, and J. L. Du, "The establishment and application of direct coupled electrostatic-structural field model in electrostatically controlled deployable membrane antenna," *Acta Astronautica*, vol. 146, pp. 185–191, 2018.
[17] Y. Rahmat-Samii, "A comparison between GO/aperture-field and physical-optics methods of offset reflectors," *IEEE Transactions on Antennas and Propagation*, vol. 32, no. 3, pp. 301–306, 1984.
[18] X. C. Wang and M. Shao, "Basic principles and numerical methods of finite element method," in *Basic Principles and Numerical Methods of Finite Element Method*. Tsinghua University Press, 1997.（in Chinese）
[19] W. T. Smith and R. J. Bastian, "An approximation of the radiation integral for distorted reflector antennas using surface-error decomposition," *IEEE Transactions on Antennas and Propagation*, vol. 45, no. 1, pp. 5–10, 1997.

Shunji ZHANG was born in Hebei Province, China, in 1994. He received the B.S. degree from Xidian University, Xi'an, China, in 2016. Now he is working towards the Ph.D. degree from the Key Laboratory of Electronic Equipment Structure Design, Ministry of Education in Xidian University, Xi'an, China. His current research interests include form-finding and structural design of deployable antennas.
(Email: zhangshunji01@126.com)

Yongzhen GU was born in Shandong Province, China, in 1991. He received the Ph.D. degree in mechanical engineering from Xidian University, China, in 2019. He is currently a M.S. Supervisor at Qingdao University of Science and Technology. His current research interests include multidisciplinary optimization, multi-physical field coupling, and structural optimization design of spaceborne antennas.
(Email: yzgu@qust.edu.cn)

Wang ZHONG was born in 1995. He received the B.S. degree from Xidian University, Xi'an, China, in 2017. Now he is currently working towards the Ph.D. degree from the Key Laboratory of Electronic Equipment Structure Design, Ministry of Education in Xidian University, Xi'an, China. His current research interests include the application of origami structure in membrane antennas.
(Email: 18792618424@163.com)

Qinggang ZHANG was born in 1997. He is currently studying for the M.S. degree at Qingdao University of Science and Technology. His research interests include optimization design of spaceborne antenna structure.
(Email: 2528909062@qq.com)